Manipulating dielectric property of polymer coatings toward high-retention-rate lithium metal full batteries under harsh critical conditions

Qi Kang[1], Zechao Zhuang[2], Yong Li[3], Yinze Zuo[4], Jian Wang[5], Yijie Liu[1], Chaoqun Shi[6], Jie Chen[1], Hongfei Li[1], Pingkai Jiang[1], and Xingyi Huang[1] (✉)

[1] *Department of Polymer Science and Engineering, Shanghai Key Laboratory of Electrical Insulation and Thermal Ageing, School of Chemistry and Chemical Engineering, Shanghai Jiao Tong University, Shanghai 200240, China*

[2] *Department of Chemistry, Tsinghua University, Beijing 100084, China*

[3] *Institute of Applied and Physical Chemistry and Center for Environmental Research and Sustainable Technology, University of Bremen, Bremen 28359, Germany*

[4] *Institute for Sustainable Energy/College of Sciences, Shanghai University, Shanghai 200444, China*

[5] *Helmholtz Institute Ulm (HIU), Ulm D89081, Germany*

[6] *School of Electrical Engineering, Xi'an Jiaotong University, Xi'an 710049, China*

ABSTRACT

Lithium (Li) metal batteries (LMBs) can potentially deliver much higher energy density but remain plagued by uncontrollable Li plating with dendrite growth, unstable interfaces, and highly abundant excess Li (> 50 mAh·cm^{-2}). Herein, different from the artificial layer or three-dimensional (3D) matrix host constructions, various dielectric polymers are initially well-comprehensively investigated from experimental characterizations to theoretical simulation to evaluate their functions in modulating Li ion distribution. As a proof of concept, a 3D interwoven high dielectric functional polymer (HDFP) nanofiber network with polar C–F dipole moments electrospun on copper (Cu) foil is designed, realizing uniform and controllable Li deposition capacity up to 5.0 mAh·cm^{-2}, thereby enabling stable Li plating/stripping cycling over 1400 h at 1.0 mA·cm^{-2}. More importantly, under the high-cathode loading (~ 3.1 mAh·cm^{-2}) and only 0.6 × excess Li (N/P ratio of 1.6), the full cells retain capacity retention of 97.4% after 200 cycles at 3.36 mA·cm^{-2} and achieve high energy density (297.7 Wh·kg^{-1} at cell-level) under lean electrolyte conditions (15 μL), much better than ever-reported literatures. Our work provides a new direction for designing high dielectric polymer coating toward high-retention-rate practical Li full batteries.

KEYWORDS

high dielectric functional polymer, nanofiber, Li metal full cell, low N/P ratio, high-retention capacity

1 Introduction

Lithium metal batteries (LMBs) arouse great attention as the next-generation energy storage system because the lithium metal anode (LMA) possesses ultrahigh theoretical specific capacity (3860 mAh·g^{-1}) and the lowest electrochemical potential (−3.04 V vs. standard hydrogen electrode) [1–8]. However, LMAs suffer from Li dendrites growth, unstable solid electrolyte interphase (SEI), and colossal volume expansion during cycling, leading to continuous consumption of the limited electrolyte, low Coulombic efficiency (CE), and depressed capacity fading [9–13]. More severely, the cycling lifespans usually become much shortened under low N/P ratio (< 3) without using excessive Li (< 10 mAh·cm^{-2}) [14].

To address these thorny issues, tremendous efforts have been made from SEI layer construction by artificial designs [15–21] or electrolyte additive engineering [22, 23] to host/current collector fabrication and modification [12, 24–27], extending the lifespan. However, most three-dimensional/two-dimensional (3D/2D) current collectors have high electrical conductivity, which inevitably leads to random Li aggregation on the top surfaces or in the edge due to the concentrated electric field [24]. Modifying the surface with ion-conductive materials seems promising to modulate the lithium behaviors to inhibit dendrite growth [27–35], especially using the ion-conductive but electronic-insulating materials [21]. Thanks to the unique properties of polymers, various organic dielectric films/hosts, such as polyimide (PI) [36], poly(dimethylsiloxane) (PDMS) [37], and β-polyvinylidene fluoride (β-PVDF) [38, 39], have been used in the LMBs and anode-free Li batteries, so as to exhibit the capability in bearing focused stress when forming dendrites. Nevertheless, tedious treatments, special nanochannel, and nonporous nature are needed to provide more pores to facilitate ion diffusion [36–38]. As pointed out by Lopez and others [40, 41], the dielectric constants of polymers can be regarded as the descriptors to evaluate their protective effect on metallic Li. However, a clear understanding of how the dielectric constants of these polymer

Address correspondence to xyhuang@sjtu.edu.cn

coatings control the deposition of Li and affect the performance of full cells has not yet been systematically investigated. In reality, there is a "trade-off" between the dielectric constant and the plating morphology [41]. For example, when the dielectric constant of polymers or their derives is too high (e.g., > 15), the transport of Li^+ might be suppressed from the electrode/electrolyte interface to Li electrode [41, 42]. The dielectric constant of a polymer is closely associated with the polar groups [43]. Thus, designing polymers with suitable groups on conductive copper (Cu) planar is the key to providing massive deposition sites and adapting large volumetric changes for achieving high-performance practical LMAs.

Herein, for the first time, various dielectric polymers employed with C=O, C≡N, and C–F polar groups on modulating Li behaviors are systematically investigated on the Cu surface. Briefly, three representative polymer nanofiber layers (e.g., low dielectric functional polymer (LDFP), medium dielectric functional polymer (MDFP), and high dielectric functional polymer (HDFP)) with C=O, C≡N, or C–F polar groups are selected as SEI layers on bare-copper (b-Cu) via electrospinning method, respectively. Interestingly, in comparison to the instability of the LDFP nanofiber employed with C=O groups when reaching the electrolyte, the MDFP and HDFP nanofibers maintain their original porous structures, homogenizing and regulating the Li-ion distribution and transport. The interwoven nanofibers not only expose massive C≡N/C–F deposition sites on the electrolyte, but also offer porous structures to accommodate large volumetric changes during the Li plating/stripping processes, so as to achieve dense and smooth LMAs. As comprehensively understood and compared by experimental results and theoretical calculations, the electroactive C–F groups will also react with Li^+ to generate a robust LiF-rich SEI layer on b-Cu foil, further increasing the dielectric constant, guiding uniform Li nucleation at the molecular level, and obtaining smooth Li deposition. Consequently, the b-Cu-HDFP/Li electrode cell can last for 1400 h and exhibit an average CE above 98.7% at 1 $mA·cm^{-2}$. More importantly, with an ultralow 0.6 × excess Li (N/P ratio of 1.6), the assembled b-Cu-HDFP/Li||NCM523 full cell with the loading of 18.69 $mg·cm^{-2}$ delivers a high capacity of 149.7 $mAh·g^{-1}$, corresponding to the areal capacity of 2.8 $mAh·cm^{-2}$ at 1.0 C (3.36 $mA·cm^{-2}$), and it manifests a 97% capacity retention after 200 cycles. Further, under harsh lean-electrolyte conditions (15 μL), the coupled full cell also shows a high-capacity retention of 90% after 100 cycles at 1.0 C. This work opens an innovative strategy of modulating the surface chemical groups with suitable dielectric constants to develop practical high-performance LMBs.

2 Results and discussion

Polymethyl methacrylate (PMMA), polyacrylonitrile (PAN), and PVDF are selected as the LDFP, MDFP, and HDFP demo with non-polar C=O, weak-polar C≡N, and strong-polar C–F groups, as shown in Fig. 1(a). Because of the employment of the C=O, C≡N, and C–F, the HDFP has the highest dielectric constant of 9.73 (@100 Hz) compared with MDFP (4.24@100 Hz) and LDFP (3.06@100 Hz) (Fig. 1(b)), indicating the strongest polarity of C–F in HDFP than C≡N in MDFP and C=O in LDFP. Although the representative polymers have different dielectric constants, all polymers are highly electrically insulating as the conductivity and dielectric loss are very low (Fig. S1 in the Electronic Supplementary Material (ESM)). X-ray photoelectron spectroscopy (XPS) analysis suggests different surface characteristics of LDFP, MDFP, and HDFP (Fig. 1(c)), including the existence of F 2s, F 1s, F KL1, F KL2, N 1s, and O 1s peaks. The C 1s spectrum of LDFP with three peaks at 284.8, 286.3, and 288.4 eV, assigned to C–C/C–H, C–O, and O–C=O bonds, respectively (Fig. 1(d)). In MDFP, deconvolution of C 1s peaks at 284.8 and 285.6 eV corresponds to C–C/C–H and C–N bonds, respectively (Fig. 1(e)) [44]. The C 1s peak for HDFP indicates the presence of –CH–, $–CH_2–$, and $–CF_2–$ with binding energies of 286.4, 287.1, and 291.5 eV, respectively (Fig. 1(f)) [45]. These results show large difference between LDFP, MDFP, and HDFP. The O 1s for LDFP, N 1s for MDFP, and F 1s for HDFP further prove their difference (Fig. S2 in the ESM).

Adsorption energies of b-Cu, LDFP, MDFP, and HDFP with Li were calculated by density functional theory (DFT) to investigate their affinity with Li. As suggested in Fig. 1(g), with the decoration of dielectric polymer, the capability of adsorbing Li atom becomes stronger. However, the HDFP shows the most negative adsorption energy of −1.44 eV toward Li^+ when compared with MDFP (−1.09 eV), LDFP (−0.66 eV), and b-Cu (−0.6 eV), indicating the highest lithiophilic property of the HDFP, which can provide more C–F sites to adsorb Li atoms due to the strong electron-withdrawing property of the F atom, further facilitating the uniform Li nucleation at the molecular level. The corresponding adsorption structures are shown in Fig. S3 in the ESM. Moreover, the differential charge transfer between Li and functional groups was also performed to further explore the Li affinity of b-Cu, LDFP, MDFP, and HDFP (inset in Fig. 1(g)). The electrons are distributed layer by layer on the b-Cu surface, indicating there is no interaction between Li and Cu. And the electrons of LDFP and MDFP are mainly localized at the Li atoms position accompanied by weak charge transfer around the O and N atoms, suggesting a weak interaction between LDFP/MDFP and Li. In contrast, the electrons of HDFP are highly localized near the binding sites, demonstrating that the F atom can adjust the electron density and bond with Li atom. All these results validate our hypothesis and provide a promising design principle to introduce a dielectric nanofiber layer for regulating Li deposition.

The b-Cu with HDFP, MDFP, and LDFP electrodes were prepared by electrospinning, respectively (Fig. 2(a)) (see details in the ESM). The optical and scanning electron microscopy (SEM) images of b-Cu are exhibited in Fig. S4 in the ESM. The color of b-Cu turns from bright yellow (Fig. S4(a) in the ESM) to well-proportioned and coherent in white after interweaving dielectric polymer, as shown in Figs. S5–S7 in the ESM. And the fabrication scale can be enlarged as desired as A4 paper (> 600 cm^2), indicating a good potential for practical application. Besides, the SEM images show the polymer nanofibers are distributed uniformly on the surface of Cu foil (Figs. 2(b), 2(d), and 2(f), and Figs. S5(b), S6(b), S7(c), and S7(d) in the ESM). The thickness of the HDFP nanofiber layer is 15 μm (Fig. S7(b) in the ESM), and the layer loading is only 0.2 $mg·cm^{-2}$, which helps enhance the energy density of LMBs. And the thicknesses of the LDFP and MDFP are also controlled to 15 μm by controlling spinning time. Compared with the b-Cu (Fig. S4(b) in the ESM), the b-Cu-polymers (Figs. 2(b), 2(d), and 2(f)) show smooth surfaces with non-polar C=O (LDFP), weak-polar C≡N (MDFP), and strong-polar C–F (HDFP) group nanofibers, which are favorable for electrochemical deposition processes.

Transmission electron microscopy (TEM) images clearly demonstrate diameters of LDFP, MDFP, and HDFP nanofibers are about 1.2 μm (Fig. 2(c)), 160 nm (Fig. 2(e)), and 360 nm (Fig. 2(g)), respectively. Moreover, the energy-dispersive X-ray (EDX) mapping images further confirm the uniform distribution of C and O elements in LDFP (Fig. 2(c)), C and N elements in MDFP (Fig. 2(e)), and C and F elements in HDFP nanofibers (Fig. 2(g)), respectively. Fourier transform infrared (FT-IR) spectroscopy was further used to confirm the existence of different functional groups from non-polar C=O to weak-polar C–N then to strong-

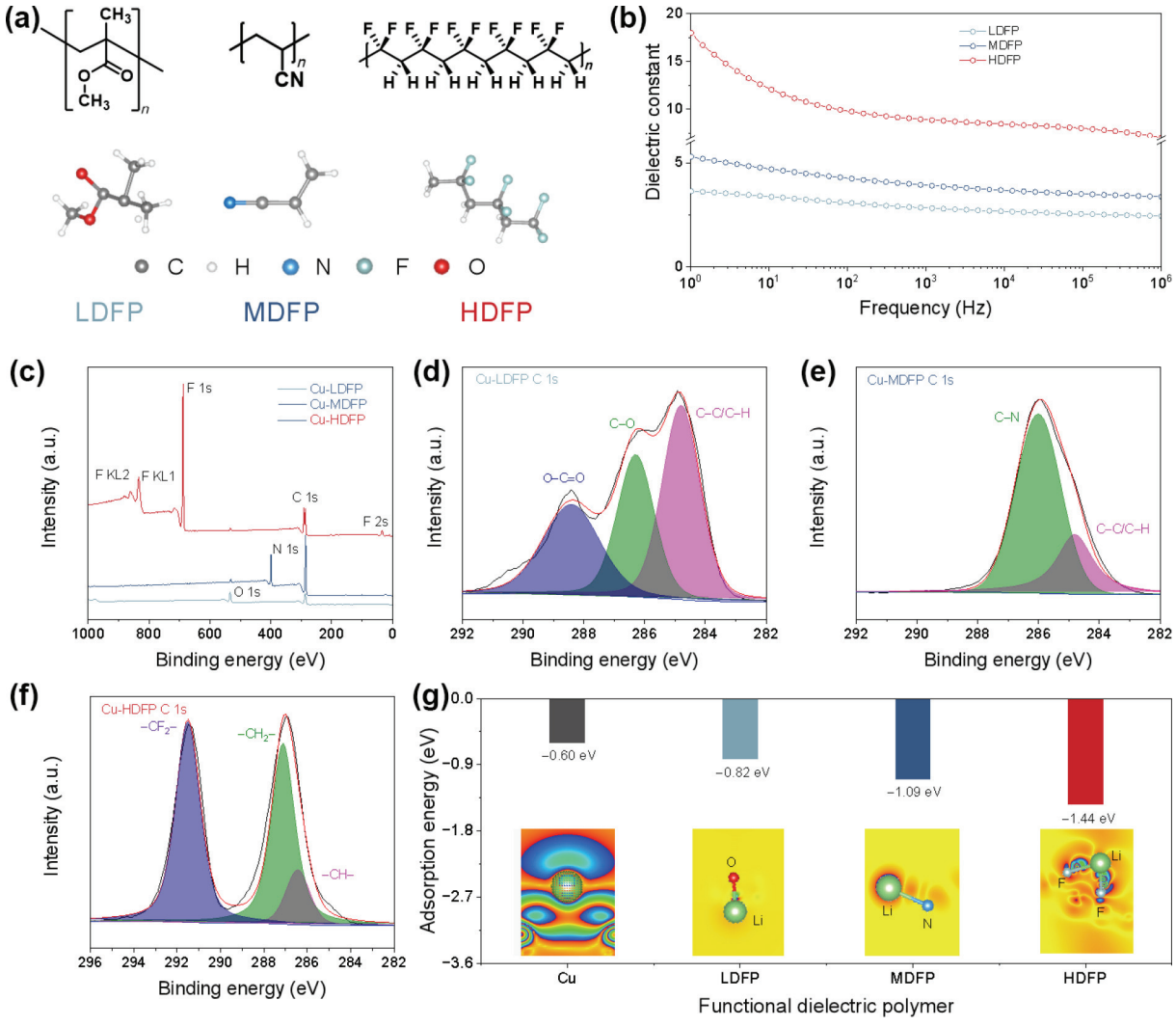

Figure 1 Properties of the LDFP, MDFP, and HDFP. (a) Chemical and molecular structures of the LDFP, MDFP, and HDFP. (b) Dielectric constants of the LDFP, MDFP, and HDFP vs. frequency. (c) XPS survey scan spectra of LDFP, MDFP, and HDFP. C 1s XPS spectra of (d) LDFP, (e) MDFP, and (f) HDFP. (g) The adsorption energies of b-Cu, b-Cu-LDFP, b-Cu-MDFP, and b-Cu-HDFP after coupled with Li atom. The insets in (g) are the corresponding 2D charge density differences of b-Cu, LDFP, MDFP, and HDFP after adsorbing one Li atom.

polar C–F groups (Fig. 2(h)). The HDFP demonstrates a dominant portion of the β-phase crystalline structure as the strong β-phase characteristic peaks appear at 510, 840, 1072, 1276, and 1431 cm^{-1} (Fig. 2(h)) [38, 39]. The β-phase has higher polarity and higher dielectric constant in comparison with the α- and γ-phase because the fluorine and hydrogen atoms in β-phase locate on opposite sides of the polymer backbone while α- and γ-phases have them in antiparallel dipole structure [39]. This β-phase HDFP nanofiber layer with highly oriented C–F groups has a good affinity with Li^+ and further enhances Li^+ transportation.

In order to investigate the Li deposition behavior on the nanofiber layers, CR-2032-coin cells were assembled using Li anodes coupled with b-Cu, b-Cu-LDFP, b-Cu-MDFP, and b-Cu-HDFP as working electrodes to deposit different amounts of Li, respectively. 1 M lithium bis(trifluoromethanesulfonyl)imide (LiTFSI) in 1,3-dioxolane (DOL)/1,2-dimethoxyethane (DME) with 2 wt.% $LiNO_3$ was used as the electrolyte. Before assembling, 10 μL electrolyte was dropped on the surfaces of b-Cu-LDFP, b-Cu-MDFP, and b-Cu-HDFP electrodes to verify the polymer stability in this electrolyte and further analyzed by SEM, as shown in Fig. S8 in the ESM. After soaking, the LDFP nanofiber disappeared and formed a dense film on the b-Cu surface (Fig. S8(a) in the ESM). The MDFP and HDFP nanofibers structures maintained their original designs (Figs. S8(b) and S8(c) in the ESM), suggesting that the medium-dielectric and high-dielectric nanofibers are more suitable to regulate Li-ion transport and guide Li deposition. Figure 3(a) shows the galvanostatic nucleation overpotential voltage profiles of asymmetric b-Cu||Li, b-Cu-LDFP||Li, b-Cu-MDFP||Li, and b-Cu-HDFP||Li at a fixed current density of 1.0 $mA{\cdot}cm^{-2}$ with a fixed plating capacity of 5.0 $mAh{\cdot}cm^{-2}$. Clearly, the b-Cu-HDFP presents the lowest nucleation onset potential (~ 36.6 mV) in comparison with the b-Cu (~ 243.3 mV), b-Cu-LDFP (~ 91.8 mV), and b-Cu-MDFP (~ 77.5 mV) (Fig. 3(b)), indicating the high lithiophilic property of HDFP nanofiber layer accompanied with a smaller charge transfer resistance. Consistent with the calculated binding energies shown in Fig. 1(g), HDFP is seen to have the lowest nucleation overpotential. Based on these experimental and theoretical results, it is believed that the HDFP nanofiber layer is a suitable material for regulating Li deposition.

Ex-situ SEM and COMSOL Multiphysics theoretical simulations (see details in Table S2 in the ESM) were further used to observe the deposited Li morphology of these four samples. The b-Cu with a low fixed capacity of Li (b-Cu/Li) presents a cobblestone-like structure firstly and further forms conglomeration with the increasing Li plating capacity (Fig. 3(c) and Fig. S9 in the ESM). However, the b-Cu/Li shows numerous grain boundaries and nonuniform Li blocks with loose structure (Fig. S9 in the ESM). More seriously, when Li plating capacity up to 5 $mAh{\cdot}cm^{-2}$, some dendritic Li appears on the surface (Fig. S9(f)

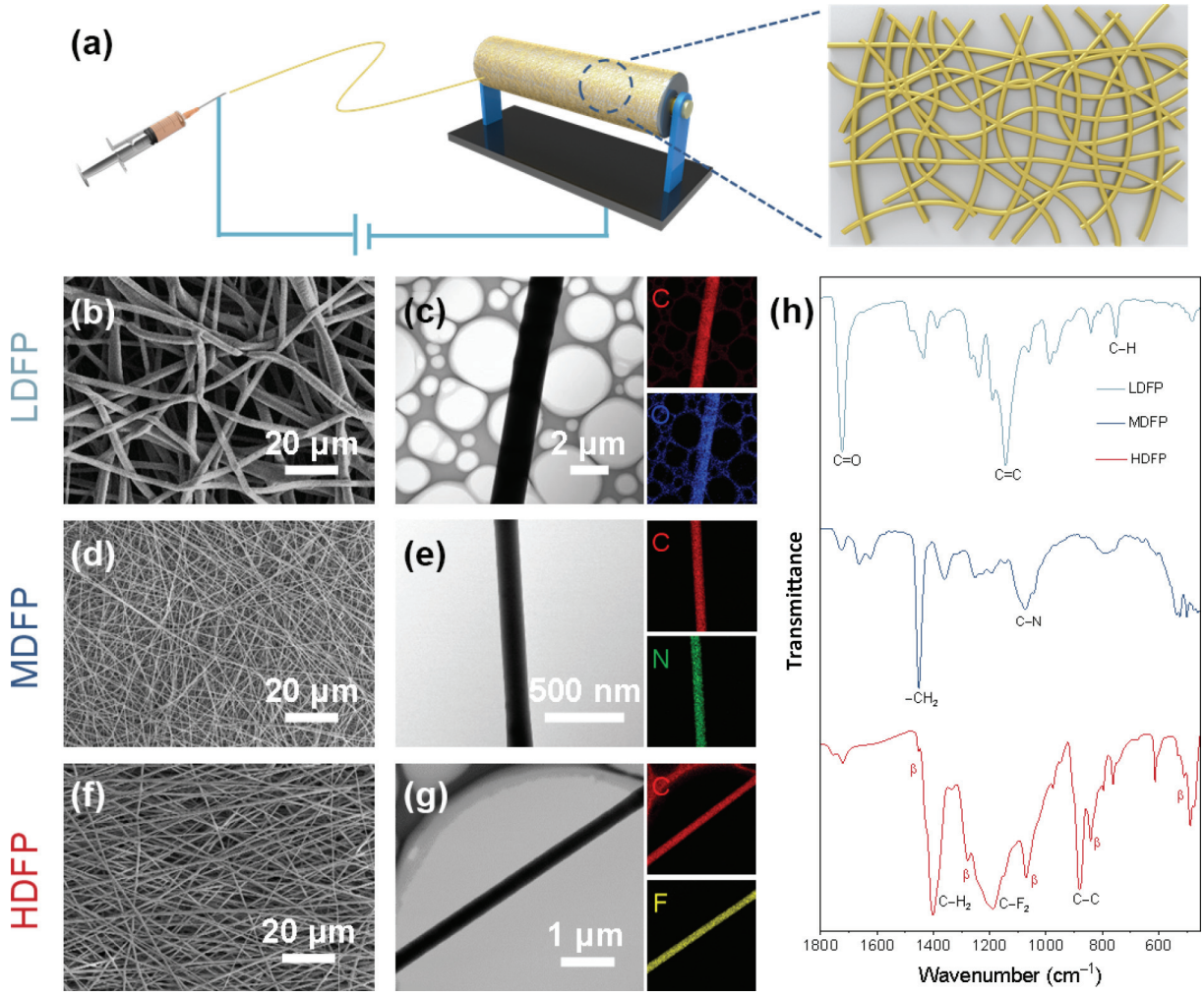

Figure 2 Preparation and characterization of the b-Cu-LDFP/MDFP/HDFP electrodes. (a) Schematic preparation of the b-Cu-LDFP/MDFP/HDFP electrodes. SEM, TEM, and EDX mapping images of the (b) and (c) LDFP, (d) and (e) MDFP, and (f) and (g) HDFP, respectively. (h) FT-IR spectra of the LDFP, MDFP, and HDFP.

in the ESM) in the outmost position (Fig. S10 in the ESM) due to the "tip effect" and nonuniform Li^+ distribution (Fig. 3(c)). When the LDFP nanofiber layer was introduced, the fiber structure disappeared because of the strong polar property of the liquid ether electrolyte and formed a dense LDFP film, thus some spherical Li particles were observed with a low fixed capacity of Li (from 0.1 to 1.0 mAh·cm^{-2}), as shown in Fig. 3(d) and Fig. S11 in the ESM. And the average intensity of the electric field with the LDFP interlayer (left part of Fig. 3(d)) was lower than b-Cu in the COMSOL simulation (left part of Fig. 3(c)). The b-Cu-LDFP with an uneven surface without Li blocks when plating 5.0 mAh·cm^{-2} (Fig. 3(d)), suggesting that the LDFP film can also guide Li deposition.

When the MDFP fiber layer was introduced, Li could easily be deposited on the MDFP fibers at a low capacity of 0.1 mAh·cm^{-2} and became denser when Li plating capacity increased (Figs. S12(a)–S12(d) in the ESM). From 1.0 to 5.0 mAh·cm^{-2}, some Li protruded from the MDFP fiber surface without obvious grain boundaries and non-uniform Li blocks (Figs. S12(c) and S12(d) in the ESM) when compared with b-Cu/Li (Figs. S9 and S10 in the ESM). However, some thorn-like projections appear on the b-Cu-MDFP/Li surface with a high capacity of 5.0 mAh·cm^{-2}, as shown in Fig. 3(e) and Fig. S12(f) in the ESM, which is attributed to the relative weak binding energy between MDFP and Li^+ (Fig. 1(g)). And the average intensity of the electric field with the MDFP interlayer (left part of Fig. 3(e)) is higher than the LDFP (left part of Fig. 3(d)) due to the relatively high dielectric constant of MDFP. In stark contrast, uniform particles are observed on the HDFP fibers surface at the early stage (0.1 mAh·cm^{-2}, Fig. S13(b) in the ESM) when compared with pure HDFP fibers (Fig. S13(a) in the ESM). After deposition for 0.5 h, Li was homogenously plated on the surface of b-Cu-HDFP (Fig. 3(f)). With more Li plating (from 0.5 to 5.0 mAh·cm^{-2}), Li was fused together and coated the entire surface of b-Cu-HDFP without any dendritic Li (Fig. 3(f) and Figs. S13(d)–S13(f) in the ESM). Notably, flat and dense Li with homogenous smooth surface (Fig. 3(f)) was achieved by using the HDFP fiber layer. Further, to reveal the lithiophilic property of the HDFP fiber layer, we used the b-Cu and b-Cu-h-HDFP (half of the HDFP fiber coating on the b-Cu) as the work electrodes to deposit Li in Li||Cu cells at 1 mA·cm^{-2} and 2 mAh·cm^{-2}, respectively. The schematic illustration of these collectors and corresponding voltage profiles of Li plating are shown in Figs. S14(a)–S14(c) in the ESM. Interestingly, comparing the Li plating curves of the b-Cu, b-Cu-h-HDFP, and b-Cu-HDFP at 1 mA·cm^{-2}, the b-Cu-HDFP shows the lowest nucleation overpotential (Fig. S14(d) in the ESM). And a uniform Li was preferentially deposited on the b-Cu-h-HDFP rather than the b-Cu due to the strong affinity between F atoms in HDFP and Li, suggesting that the HDFP nanofibers can supply plenty of lithiophilic sites to guide Li nucleation and growth (Figs. S14(e) and S14(f) in the ESM). And the average intensity of the electric field with the HDFP interlayer (left part of Fig. 3(f)) is the highest when compared with LDFP (left part of Fig. 3(d)) and MDFP (left part of Fig. 3(e)) layers but is still lower than the b-Cu (left part of Fig. 3(c)). These results clearly reveal that the HDFP fiber layer can redistribute the access of Li^+ and is suitable for preparing dendrite-free Li anodes.

Based on these results and understanding, we propose the

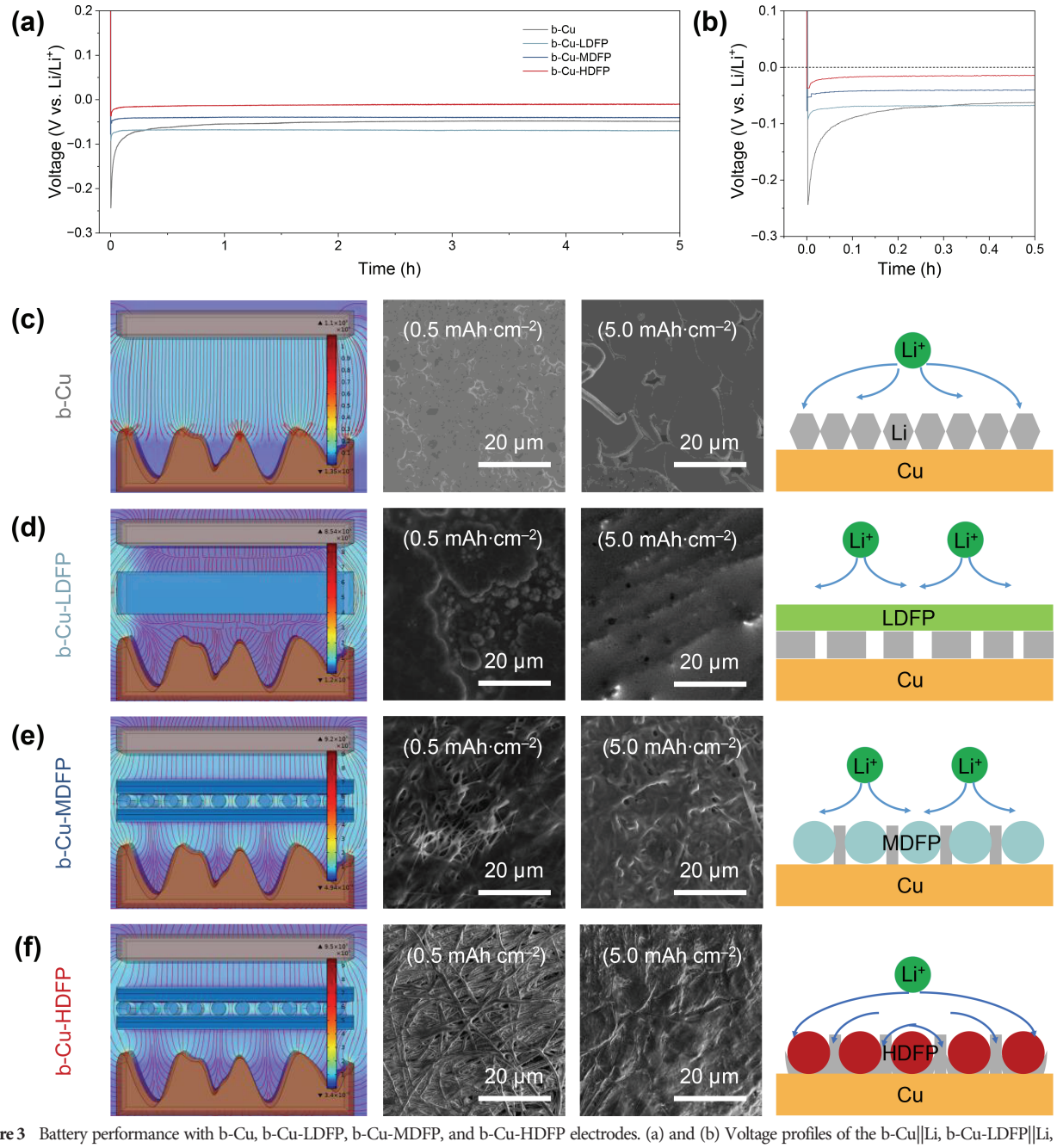

Figure 3 Battery performance with b-Cu, b-Cu-LDFP, b-Cu-MDFP, and b-Cu-HDFP electrodes. (a) and (b) Voltage profiles of the b-Cu||Li, b-Cu-LDFP||Li, b-Cu-MDFP||Li, and b-Cu-HDFP||Li cells at 1 mA·cm^{-2}. COMSOL simulation, SEM images, and schematic mechanism of Li deposition models on (c) b-Cu, (d) b-Cu-LDFP, (e) b-Cu-MDFP, and (f) b-Cu-HDFP surfaces.

possible Li deposition models on the b-Cu and b-Cu-LDFP/MDFP/HDFP nanofiber layers (right half parts of Figs. 3(c)–3(f)). On the b-Cu surface, due to the "tip effect" caused by the defects on Cu foils, a high local electrical field is generated on the micro-bulges, leading to nonuniform Li^+ flux distribution and deposition (right half of Fig. 3(c)). Moreover, with the continuous consumption of Li^+ near the bulged surfaces, the Li tends to deposit with a dendritic structure at a high deposited capacity. Introducing the LDFP nanofiber layer, the ion-transport channel was blocked because the LDFP fibers were dissolved and formed a dense film. Thus, the Li^+ is challenging to transport through the LDFP film. The possible deposition model is shown in the right half of Fig. 3(d). However, introducing the MDFP nanofiber layer provides a relatively weak dipole to interact with Li^+, further guiding Li deposition along the MDFP nanofiber surface (right half of Fig. 3(e)). On the contrary, HDFP layer offers strong dipoles along its nanofibers, providing enough deposition sites and enabling Li^+ flux through the HDFP nanofiber layer (right half of Fig. 3(f)). Moreover, the high lithiophilic property of HDFP nanofiber layer alleviates the irregularity of local Li^+ concentrations on the b-Cu-HDFP surface via spreading out Li^+ pathways along the polar HDFP fibers, resulting in lower nucleation overpotential and uniform Li deposition. These results imply that the thin HDFP nanofiber layer is the key to inducing dendrite-free Li deposition owing to its highest dielectric constant and relatively uniform distribution of both Li^+ flux and electronic field, which will significantly improve the electrochemical performance of the b-Cu-HDFP/Li anodes in the full LMBs.

XPS was further applied to investigate the chemical composition of the deposited surface of the b-Cu/Li, b-Cu-MDFP/Li, and b-Cu-HDFP/Li (Fig. S15 in the ESM). The deconvolution of the Li 1s of b-Cu/Li shows three peaks at 52.9, 54.5, and 55.7 eV, which can be assigned to interstitial Li (Li defects), Li/LiOH, and Li_2O species, respectively (Fig. S15(a) in the ESM) [46]. In the C 1s spectrum, only one peak of C–C specie originates from the decomposition of the electrolyte. And a weak

signal of N 1s can also be observed. The C 1s peak for b-Cu-MDFP/Li shows the presence of C–C and C–N with binding energies of 284.8 and 286.2 eV, respectively (Fig. S15(b) in the ESM). But the Li 1s peaks at 56.2 and 57.2 eV correspond to LiF and Li–N species [47], indicating the weak couple interaction between MDFP and Li^+, which is in agreement with the DFT calculation result (Fig. 1(g)). And the signal of N 1s is strong due to the high N content ratio in the MDFP. In comparison, the C 1s peaks of the b-Cu-HDFP/Li assigned to C–C, C–F, $–CH_2–CF_2–$, and CF_3 at 284.8, 286, 290.5, and 293.2 eV generated from the HDFP fiber [1], respectively (Fig. S15(c) in the ESM). Similar to the b-Cu/Li, the N 1s signal of b-Cu-HDFP/Li is also weak because there is no N-containing in the b-Cu and b-Cu-HDFP. In addition, the Li 1s spectrum shows three peaks at 55.2, 56.2, and 59.0 eV, corresponding to Li/LiOH, LiF, and Li–C species, respectively. The formation of high content ratio LiF indicates the chemical couple reaction between F atoms in HDFP with Li^+ in the liquid electrolyte, consistent with the simulated DFT prediction (Fig. 1(g)). The formed LiF can effectively protect the b-Cu-HDFP/Li anode, reducing undesirable side reactions and improving Li^+ diffusion through the b-Cu-HDFP/Li-LiF interphase.

Considering Li reversibility is the most crucial parameter for practical LMBs to reflect the sustainability and efficiency of the LMAs, continuous Li plating/stripping experiments were carried out in the b-Cu||Li, b-Cu-LDFP||Li, b-Cu-MDFP||Li, and b-Cu-HDFP||Li cells. The electrochemical impedance spectroscopy (EIS) plots (Fig. 4(a)) demonstrate that the b-Cu-HDFP||Li exhibits the smallest charge-transfer resistance when compared with the b-Cu||Li, b-Cu-LDFP||Li, and b-Cu-HDFP||Li cells, indicating the correlation between the HDFP fiber layer and Li deposition kinetics. Furthermore, the HDFP nanofiber layer homogenizes the local electric field because of its high lithiophilic and high-dielectric nature, which accelerates Li^+ flux transportation and reduces the nucleation potential. As shown in Figs. S8(a)–S8(c) in the ESM, the LDFP nanofibers were dissolved by the electrolyte (LiTFSI, DOL/DME + $LiNO_3$) and formed dense LDFP film without enough nanopores to transport Li ions, thus the charge-transfer resistance of b-Cu-LDFP||Li cell is only slightly larger than the b-Cu||Li cell.

CE is usually used to evaluate the practicality and sustainability of the LMAs, which is defined as the ratio of stripped capacity to plated capacity in the Cu||Li half cell. The results are plotted as CE versus cycle number of cells at 1 mA·cm^{-2} with the plating capacity of 1 mAh·cm^{-2}, as illustrated in Fig. 4(b). Specially, the b-Cu-HDFP||Li cell exhibits stable CE of 98.7% over 230 cycles, however, the b-Cu||Li, b-Cu-LDFP||Li, and b-Cu-MDFP||Li cells exhibit CEs of 89.5%, 82.5%, and 94.4% after 89, 120, and 170 cycles, respectively (Fig. S16 in the ESM). These results fully indicate the b-Cu with HDFP nanofiber coating can greatly improve the CEs and extend the cycling life of half cells when compared with LDFP and MDFP nanofiber coating, which can be assigned to high adsorption energy between C–F groups in HDFP with Li^+ in electrolyte.

Reversible Li plating and stripping were further evaluated in symmetric cells. First, 5 mAh·cm^{-2} Li was deposited on b-Cu, b-Cu-LDFP, b-Cu-MDFP, and b-Cu-HDFP electrodes to obtain the b-

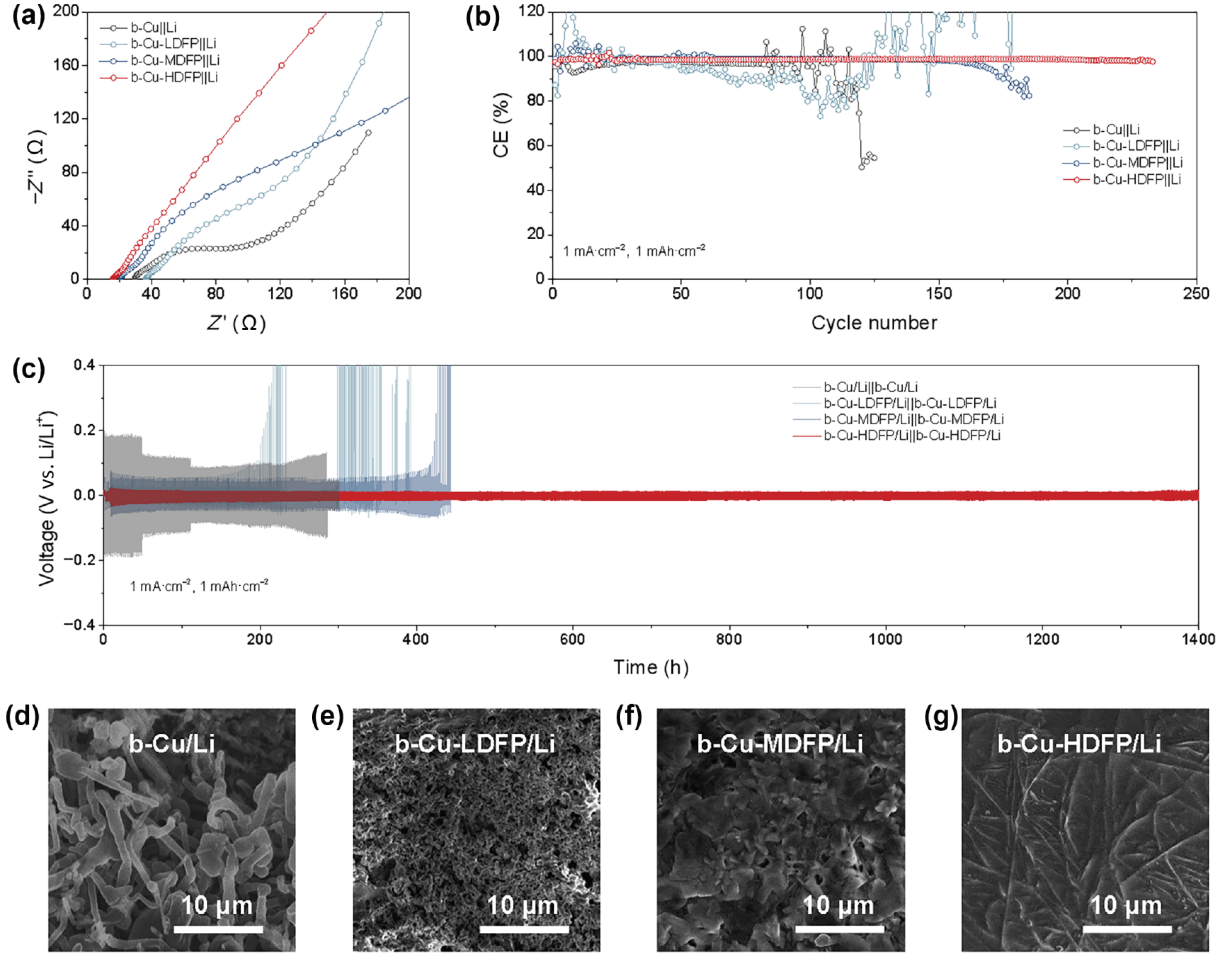

Figure 4 Electrical performances of the asymmetric and symmetric cells. (a) EIS curves of the b-Cu||Li, b-Cu-LDFP||Li, b-Cu-MDFP||Li, and b-Cu-HDFP||Li cells. (b) CEs tests of b-Cu, b-Cu-LDFP, b-Cu-MDFP, and b-Cu-HDFP electrodes. (c) Galvanostatic Li plating/stripping voltage profiles for b-Cu/Li||b-Cu/Li, b-Cu-LDFP/Li||b-Cu-LDFP/Li, b-Cu-MDFP/Li||b-Cu-MDFP/Li, and b-Cu-HDFP/Li||b-Cu-HDFP/Li symmetric cells at 1 mA·cm^{-2} and 1 mAh·cm^{-2}. SEM images of (d) b-Cu/Li, (e) b-Cu-LDFP/Li, (f) b-Cu-MDFP/Li, and (g) b-Cu-HDFP/Li after cycling.

Cu/Li, b-Cu-LDFP/Li, b-Cu-MDFP/Li, and b-Cu-HDFP/Li anodes, respectively. Then b-Cu/Li||b-Cu/Li, b-Cu-LDFP/Li||b-Cu-LDFP/Li, b-Cu-MDFP/Li||b-Cu-MDFP/Li, and b-Cu-HDFP/Li||b-Cu-HDFP/Li cells were assembled to test long-term cycling at 1 mA·cm^{-2} and 1 mAh·cm^{-2}, respectively. The b-Cu-HDFP/Li||b-Cu-HDFP/Li displays steady cyclability over 1400 h with a small overpotential of 15 mV (Fig. 4(c)). By contrast, the b-Cu/Li||b-Cu/Li, b-Cu-LDFP/Li||b-Cu-LDFP/Li, and b-Cu-MDFP/Li||b-Cu-MDFP/Li cells show an overpotential over 100 mV after 10, 210, and 450 h, respectively. The b-Cu-HDFP/Li||b-Cu-HDFP/Li cell possesses the lowest hysteresis voltage due to the lithiophilic HDFP nanofiber layer with fast Li^+ flux transportation and b-Cu-HDFP/Li-LiF interphase. After cycling, b-Cu/Li shows obvious wire-shaped Li dendrites (Fig. 4(d)), whereas b-Cu-LDFP/Li and b-Cu-MDFP/Li exhibit an uneven and loose surface without dendrites, respectively, as shown in Figs. 4(e) and 4(f). On the contrary, b-Cu-HDFP/Li displays a very flat and dense surface (Fig. 4(g)), indicating the stable interphase and excellent reproducibility during cycling. Therefore, it can be concluded that this HDFP nanofiber layer can effectively regulate the Li deposition behavior, homogenize the electric field, and stabilize the Li anodes interphase.

The electrochemical performance of b-Cu/Li, b-Cu-HDFP/Li, b-Cu-MDFP/Li, and b-Cu-HDFP/Li anodes were further evaluated in coin-full cells paired with high-loading $LiNi_{0.5}Co_{0.2}Mn_{0.3}O_2$ (NCM523) (3.2 mAh·cm^{-2}, Fig. S17 in the ESM) cathodes at a low N/P ratio of 1.6. Before cycling, EIS curves of the b-Cu/Li||NCM523, b-Cu-HDFP/Li||NCM523, b-Cu-MDFP/Li||NCM523, and b-Cu-HDFP/Li||NCM523 full cells were tested (Fig. S18 in the ESM). Obviously, the b-Cu-HDFP/Li||NCM523 displays the smallest internal and transfer-charge resistance when compared with the b-Cu/Li||NCM523, b-Cu-LDFP/Li||NCM523, and b-Cu-MDFP/Li||NCM523 full cells (Fig. S18 in the ESM), indicating the fast Li^+ transportation through the b-Cu-HDFP/Li-LiF interphase and high affinity of b-Cu-HDFP/Li anode with the liquid carbonate electrolyte.

The assembled b-Cu/Li||NCM523, b-Cu-LDFP/Li||NCM523, b-Cu-MDFP/Li||NCM523, and b-Cu-HDFP/Li||NCM523 full cells were cycled from 3.0 to 4.3 V with initial four activation cycles at 0.1/0.1, 0.5/0.1, 0.5/0.2, and 0.5/0.5 C, respectively (Fig. S19 in the ESM). The b-Cu/Li||NCM523 full cell exhibits fast capacity fading (Fig. 5(a)) and low capacity retention (28.7% after 50 cycles) at 1.0 C (3.36 mA·cm^{-2}), which is mainly attributed to the side reaction between b-Cu/Li and carbonate electrolyte. The corresponding voltage profiles from the 1st and 200th cycles are shown in Fig. S20(a) in the ESM. Whereas the b-Cu-LDFP/Li||NCM523 and b-Cu-MDFP/Li||NCM523 full cells deliver a relatively higher capacity retention (68.7% and 92.3% after 100 cycles, respectively) and drop quickly after 100 cycles (Fig. 5(a), and Figs. S20(b) and S20(c) in the ESM), Both the b-Cu/Li||NCM523, b-Cu-LDFP/Li||NCM523, and b-Cu-MDFP/Li||NCM523 full cells show sudden fluctuations in CEs (Fig. 5(a)). By contrast, the b-Cu-HDFP/Li||NCM523 presents the highest capacity retention (97.4% after 200 cycles) and steady CEs (Fig. 5(a)). With the consumption of liquid electrolytes, the overpotential increases slightly but keeps a high specific capacity (Fig. S20(d) in the ESM).

Rate performance of these three full cells was also investigated at different rates from 0.1 to 5.0 C (16.84 mA·cm^{-2}), as shown in Fig. 5(b). The b-Cu-HDFP/Li||NCM523 full cell delivers higher specific capacities of 164.2, 162.9, 159.7, 152.3, 140.2, 121.7, 88, and 50.8 mAh·g^{-1} at 0.1, 0.2, 0.5, 1.0, 2.0, 3.0, 4.0, and 5.0 C when compared with the b-Cu/Li||NCM523, b-Cu-LDFP/Li||NCM523, and b-Cu-MDFP/Li||NCM523 full cells, respectively (Fig. 5(b) and Fig. S21 in the ESM). And the performance of the b-Cu-HDFP/Li||NCM523 full cell with a low N/P ratio of 1.6 delivers higher capacity retention (97.4% after 200 cycles) with the highest cathode loading when compared with the previous reported full cells (Fig. 5(c) and Table S3 in the ESM) [11, 48–56]. Even under lean electrolyte condition (15 μL), the b-Cu-HDFP/Li||NCM523 full cell manifests a high specific capacity of 150.4 mAh·g^{-1} with a capacity retention of 90.0% after 100 cycles (Fig. 5(d) and Fig. S22 in the ESM). And this coin-cell offers a high gravimetric energy density of 297.9 Wh·kg^{-1} (Table S4 in the ESM).

After cycling at 1.0 C for 200 cycles, the NCM523 cathode keeps the complete structure without obvious change (Fig. S23 in the ESM) compared with that before cycling (Fig. S17 in the ESM). Thus, the capacity fading in b-Cu/Li||NCM523, b-Cu-LDFP/Li||NCM523, and b-Cu-MDFP/Li||NCM523 full cells was mainly ascribed to the poor stability of b-Cu/Li, b-Cu-LDFP/Li, and b-Cu-MDFP/Li anodes (Fig. 5(e) and Figs. S24(a)–S24(i) in the ESM). And the b-Cu-HDFP/Li anode shows dense and smooth morphology after cycling at 1.0 C for 200 cycles (Figs. S24(j)–S24(l) in the ESM), indicating excellent interfacial stability in full cells for long-term circulation. Furthermore, the b-Cu-HDFP/Li||NCM811 full cell with high capacity $LiNi_{0.8}Co_{0.1}Mn_{0.1}O_2$ (NCM811) cathode (4.28 mAh·cm^{-2}) shows a high-capacity retention of 90.4% after 50 cycles at 1.32 mA·cm^{-2} with a low N/P (1.16) and lean condition (15 μL) (Fig. 5(f) and Fig. S25 in the ESM), and reaches a high energy density of 382.4 Wh·kg^{-1} at cell-level (Table S4 in the ESM), demonstrating the full functional features of the b-Cu-HDFP/Li. These results suggest that the high-dielectric fiber layer ensures the stable electrolyte/electrode interphase and high reversibility, and exhibits potential application for high-energy LMBs.

3 Conclusions

In summary, a series of chemical groups of C=O in LDFP, weak-polar C≡N in MDFP, and strong-polar C–F in HDFP contributing to different dielectric constants are well-comprehensively investigated in modulating Li ion behaviors from experimental characterizations to theoretical simulations. The designed high dielectric functional polymer nanofiber coating on Cu exhibits highly polarized C–F groups, interwoven network, and high lithiophilic property to improve the cycling stability of Li anode. This optimized HDFP nanofiber with long-range-ordered dipole moments effectively homogenizes Li^+ flux, forms stable LiF-enrich interphase, and accommodates large volumetric changes, facilitating long-term cycling stability over 1400 h at 1 mA·cm^{-2}. Moreover, with 0.6 × excess Li (N/P ratio of 1.6), the b-Cu-HDFP/Li||NCM523 full cell delivers a capacity retention of 97.4% after 200 cycles at 1.0 C, which is superior to the ever-reported ones. Under realistic electrolyte conditions (15 μL), the full cell manifests a high-capacity retention (90%) after 100 cycles at 1.0 C and achieves a high energy density of 297.9 Wh·kg^{-1} at cell-level. This work provides a new strategy to design high-performance full cells with limited excessive Li by employing high dielectric functional polymer nanofiber coating for practical applications.

Acknowledgements

This work was financial supported by the National Natural Science Foundation of China (Nos. 51877132, 52003153, and 22005186) and the Program of Shanghai Academic Research Leader (No. 21XD1401600).

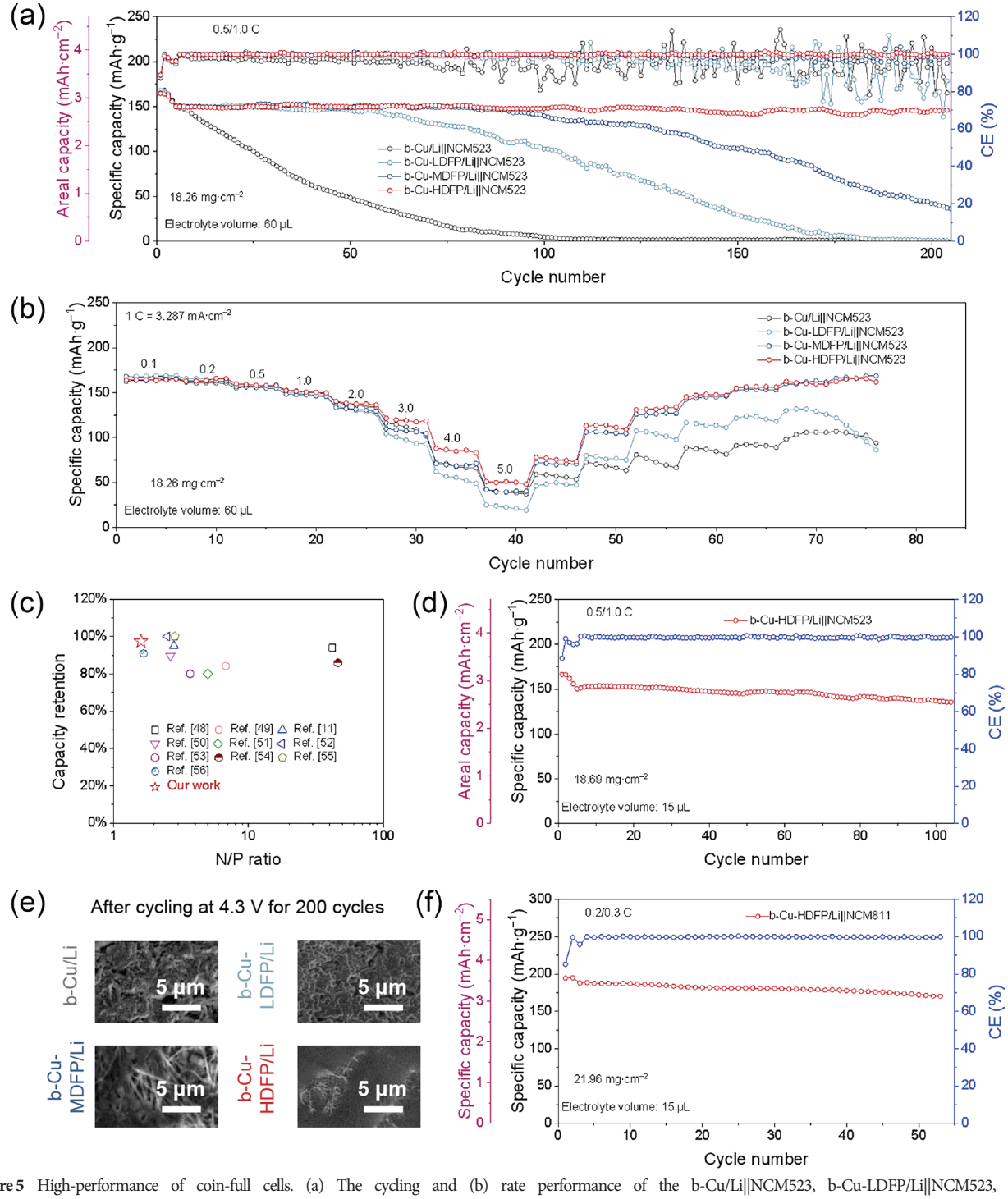

Figure 5 High-performance of coin-full cells. (a) The cycling and (b) rate performance of the b-Cu/Li||NCM523, b-Cu-LDFP/Li||NCM523, b-Cu-MDFP/Li||NCM523, and b-Cu-HDFP/Li||NCM523 with only 0.6 × excess Li anodes. (c) Comparison of capacity retention of b-Cu-HDFP/Li and previous reported full cell with different N/P ratios [11, 48–56]. (d) The cycling performance of the b-Cu-HDFP/Li||NCM523 full cell under the lean-electrolyte condition (15 μL). (e) SEM images of the b-Cu/Li, b-Cu-LDFP/Li, b-Cu-MDFP/Li, and b-Cu-HDFP/Li anodes after cycling. (f) Cycling performance of the b-Cu-HDFP/Li||NCM811 full cell with an ultralow N/P ratio (1.16). Note: the mass loadings of NCM523 and NCM811 are 18.69 and 21.96 mg·cm^{-2}, respectively.

References

[1] Liu, Y. J.; Tao, X. Y.; Wang, Y.; Jiang, C.; Ma, C.; Sheng, O. W.; Lu, G. X.; Lou, X. W. D. Self-assembled monolayers direct a LiF-rich interphase toward long-life lithium metal batteries. *Science* **2022**, *375*, 739–745.

[2] Wang, J.; Li, L. G.; Hu, H. M.; Hu, H. F.; Guan, Q. H.; Huang, M.; Jia, L. J.; Adenusi, H.; Tian, K. V.; Zhang, J. et al. Toward dendrite-free metallic lithium anodes: From structural design to optimal electrochemical diffusion kinetics. *ACS Nano,* **2022**, *16*, 17729–17760.

[3] Kang, Q.; Li, Y.; Zhuang, Z. C.; Wang, D. S.; Zhi, C. Y.; Jiang, P. K.; Huang, X. Y. Dielectric polymer based electrolytes for high-performance all-solid-state lithium metal batteries. *J. Energy Chem.* **2022**, *69*, 194–204.

[4] Um, J. H.; Yu, S. H. Unraveling the mechanisms of lithium metal plating/stripping via *in situ*/*operando* analytical techniques. *Adv. Energy Mater.* **2021**, *11*, 2003004.

[5] Zhang, W. D.; Zhang, S. Q.; Fan, L.; Gao, L. N.; Kong, X. Q.; Li, S. Y.; Li, J.; Hong, X.; Lu, Y. Y. Tuning the LUMO energy of an organic interphase to stabilize lithium metal batteries. *ACS Energy Lett.* **2019**, *4*, 644–650.

[6] Wang, J.; Zhang, J.; Duan, S. R.; Jia, L. J.; Xiao, Q. B.; Liu, H. T.; Hu, H. M.; Cheng, S.; Zhang, Z. Y.; Li, L. G. et al. Lithium atom surface diffusion and delocalized deposition propelled by atomic metal catalyst toward ultrahigh-capacity dendrite-free lithium anode. *Nano Lett.* **2022**, *22*, 8008–8017.

[7] Wang, J.; Zhang, J.; Cheng, S.; Yang, J.; Xi, Y. L.; Hou, X. G.; Xiao, Q. B.; Lin, H. Z. Long-life dendrite-free lithium metal electrode achieved by constructing a single metal atom anchored in a diffusion modulator layer. *Nano Lett.* **2021**, *21*, 3245–3253.

[8] Wang, D.; Liu, Y. M.; Li, G. W.; Qin, C. C.; Huang, L.; Wu, Y. P. Liquid metal welding to suppress Li dendrite by equalized heat distribution. *Adv. Funct. Mater.* **2021**, *31*, 2106740.

[9] Wang, S. Y.; Wang, Z. W.; Chen, F. Z.; Peng, B.; Xu, J.; Li, J. Z.; Lv, Y. H.; Kang, Q.; Xia, A. L.; Ma, L. B. Electrocatalysts in lithium-sulfur batteries. *Nano Res.*, in press, https://doi.org/10.1007/s12274-022-5215-4.

[10] Hu, B.; Xu, J.; Fan, Z.; Xu, C.; Han, S.; Zhang, J.; Ma, L.; Ding, B.; Zhuang, Z.; Kang, Q. et al. Covalent organic framework-based lithium-sulfur batteries: Materials, interfaces, and solid-state electrolytes. *Adv. Energy Mater.*, in press, https://doi.org/10.1002/aenm.202203540.

[11] Sun, H.; Zhu, G. Z.; Zhu, Y. M.; Lin, M. C.; Chen, H.; Li, Y. Y.; Hung, W. H.; Zhou, B.; Wang, X.; Bai, Y. X. et al. High-safety and high-energy-density lithium metal batteries in a novel ionic-liquid electrolyte. *Adv. Mater.* **2020**, *32*, 2001741.

[12] Pei, F.; Fu, A.; Ye, W. B.; Peng, J.; Fang, X. L.; Wang, M. S.; Zheng, N. F. Robust lithium metal anodes realized by lithiophilic 3D porous current collectors for constructing high-energy lithium-sulfur batteries. *ACS Nano* **2019**, *13*, 8337–8346.

[13] Yang, H. J.; Qiao, Y.; Chang, Z.; Deng, H.; He, P.; Zhou, H. S. A safe and sustainable lithium-ion-oxygen battery based on a low-cost dual-carbon electrodes architecture. *Adv. Mater.* **2021**, *33*, 2100827.

[14] Shi, P.; Zhang, X. Q.; Shen, X.; Zhang, R.; Liu, H.; Zhang, Q. A review of composite lithium metal anode for practical applications. *Adv. Mater. Technol.* **2020**, *5*, 1900806.

[15] Xu, S. M.; Duan, H.; Shi, J. L.; Zuo, T. T.; Hu, X. C.; Lang, S. Y.; Yan, M.; Liang, J. Y.; Yang, Y. G.; Kong, Q. H. et al. *In situ* fluorinated solid electrolyte interphase towards long-life lithium metal anodes. *Nano Res.* **2020**, *13*, 430–436.

[16] Liu, S. F.; Ji, X.; Yue, J.; Hou, S.; Wang, P. F.; Cui, C. Y.; Chen, J.; Shao, B. W.; Li, J. R.; Han, F. D. et al. High interfacial-energy interphase promoting safe lithium metal batteries. *J. Am. Chem. Soc.* **2020**, *142*, 2438–2447.

[17] Kim, M. S.; Ryu, J. H.; Deepika; Lim, Y. R.; Nah, I. W.; Lee, K. R.; Archer, L. A.; Il Cho, W. Langmuir–Blodgett artificial solid–electrolyte interphases for practical lithium metal batteries. *Nat. Energy* **2018**, *3*, 889–898.

[18] Li, F.; He, J.; Liu, J. D.; Wu, M. G.; Hou, Y. Y.; Wang, H. P.; Qi, S. H.; Liu, Q. H.; Hu, J. W.; Ma, J. M. Gradient solid electrolyte interphase and lithium-ion solvation regulated by bisfluoroacetamide for stable lithium metal batteries. *Angew. Chem., Int. Ed.* **2021**, *60*, 6600–6608.

[19] Wang, Y. Y.; Wang, Z. J.; Zhao, L.; Fan, Q. N.; Zeng, X. H.; Liu, S. L.; Pang, W. K.; He, Y. B.; Guo, Z. P. Lithium metal electrode with increased air stability and robust solid electrolyte interphase realized by silane coupling agent modification. *Adv. Mater.* **2021**, *33*, 2008133.

[20] Liu, F. F.; Wang, L. F.; Zhang, Z. W.; Shi, P. C.; Feng, Y. Z.; Yao, Y.; Ye, S. F.; Wang, H. Y.; Wu, X. J.; Yu, Y. A mixed lithium-ion conductive Li_2S/Li_2Se protection layer for stable lithium metal anode. *Adv. Funct. Mater.* **2020**, *30*, 2001607.

[21] Xu, R.; Cheng, X. B.; Yan, C.; Zhang, X. Q.; Xiao, Y.; Zhao, C. Z.; Huang, J. Q.; Zhang, Q. Artificial interphases for highly stable lithium metal anode. *Matter* **2019**, *1*, 317–344.

[22] Piao, N.; Liu, S. F.; Zhang, B.; Ji, X.; Fan, X. L.; Wang, L.; Wang, P. F.; Jin, T.; Liou, S. C.; Yang, H. C. et al. Lithium metal batteries enabled by synergetic additives in commercial carbonate electrolytes. *ACS Energy Lett.* **2021**, *6*, 1839–1848.

[23] Fu, J. L.; Ji, X.; Chen, J.; Chen, L.; Fan, X. L.; Mu, D. B.; Wang, C. S. Lithium nitrate regulated sulfone electrolytes for lithium metal batteries. *Angew. Chem., Int. Ed.* **2020**, *59*, 22194–22201.

[24] Li, J.; Zou, P. C.; Chiang, S. W.; Yao, W. T.; Wang, Y.; Liu, P.; Liang, C. W.; Kang, F. Y.; Yang, C. A conductive-dielectric gradient framework for stable lithium metal anode. *Energy Storage Mater.* **2020**, *24*, 700–706.

[25] Chen, C.; Guan, J.; Li, N. W.; Lu, Y.; Luan, D. Y.; Zhang, C. H.; Cheng, G.; Yu, L.; Lou, X. W. Lotus-root-like carbon fibers embedded with Ni-Co nanoparticles for dendrite-free lithium metal anodes. *Adv. Mater.* **2021**, *33*, 2100608.

[26] Zhang, K.; Liu, W.; Gao, Y. L.; Wang, X. W.; Chen, Z. X.; Ning, R. Q.; Yu, W.; Li, R. L.; Li, L.; Li, X. et al. A high-performance lithium metal battery with ion-selective nanofluidic transport in a conjugated microporous polymer protective layer. *Adv. Mater.* **2021**, *33*, 2006323.

[27] Chen, H.; Yang, Y. F.; Boyle, D. T.; Jeong, Y. K.; Xu, R.; de Vasconcelos, L. S.; Huang, Z. J.; Wang, H. S.; Wang, H. X.; Huang, W. X. et al. Free-standing ultrathin lithium metal-graphene oxide host foils with controllable thickness for lithium batteries. *Nat. Energy* **2021**, *6*, 790–798.

[28] Qian, J.; Wang, S.; Li, Y.; Zhang, M. L.; Wang, F. J.; Zhao, Y. Y.; Sun, Q.; Li, L.; Wu, F.; Chen, R. J. Lithium induced nano-sized copper with exposed lithiophilic surfaces to achieve dense lithium deposition for lithium metal anode. *Adv. Funct. Mater.* **2021**, *31*, 2006950.

[29] Sun, C. Z.; Li, Y. P.; Jin, J.; Yang, J. H.; Wen, Z. Y. ZnO nanoarray-modified nickel foam as a lithiophilic skeleton to regulate lithium deposition for lithium-metal batteries. *J. Mater. Chem. A* **2019**, *7*, 7752–7759.

[30] Yue, X. Y.; Li, X. L.; Wang, W. W.; Chen, D.; Qiu, Q. Q.; Wang, Q. C.; Wu, X. J.; Fu, Z. W.; Shadike, Z.; Yang, X. Q. et al. Wettable carbon felt framework for high loading Li-metal composite anode. *Nano Energy* **2019**, *60*, 257–266.

[31] Cheng, Q.; Li, A. J.; Li, N.; Li, S.; Zangiabadi, A.; Li, T. D.; Huang, W. L.; Li, A. C.; Jin, T. W.; Song, Q. Q. et al. Stabilizing solid electrolyte–anode interface in Li-metal batteries by boron nitride-based nanocomposite coating. *Joule* **2019**, *3*, 1510–1522.

[32] Yan, K.; Lu, Z. D.; Lee, H. W.; Xiong, F.; Hsu, P. C.; Li, Y. Z.; Zhao, J.; Chu, S.; Cui, Y. Selective deposition and stable encapsulation of lithium through heterogeneous seeded growth. *Nat. Energy* **2016**, *1*, 16010.

[33] Cui, Y. L.; Liu, S. F.; Wang, D. H.; Wang, X. L.; Xia, X. H.; Gu, C. D.; Tu, J. P. A facile way to construct stable and ionic conductive lithium sulfide nanoparticles composed solid electrolyte interphase on Li metal anode. *Adv. Funct. Mater.* **2021**, *31*, 2006380.

[34] Huang, Z. J.; Zhang, C.; Lv, W.; Zhou, G. M.; Zhang, Y. B.; Deng, Y. Q.; Wu, H. L.; Kang, F. Y.; Yang, Q. H. Realizing stable lithium deposition by *in situ* grown Cu_2S nanowires inside commercial Cu foam for lithium metal anodes. *J. Mater. Chem. A* **2019**, *7*, 727–732.

[35] Lu, Y. Z.; Wang, J. S.; Chen, Y.; Zheng, X. Y.; Yao, H. R.; Mathur, S.; Hong, Z. S. Spatially controlled lithium deposition on silver-nanocrystals-decorated TiO_2 nanotube arrays enabling ultrastable lithium metal anode. *Adv. Funct. Mater.* **2021**, *31*, 2009605.

[36] Liu, W.; Lin, D. C.; Pei, A.; Cui, Y. Stabilizing lithium metal anodes by uniform Li-ion flux distribution in nanochannel confinement. *J. Am. Chem. Soc.* **2016**, *138*, 15443–15450.

[37] Zhu, B.; Jin, Y.; Hu, X. Z.; Zheng, Q. H.; Zhang, S.; Wang, Q. J.; Zhu, J. Poly(dimethylsiloxane) thin film as a stable interfacial layer for high-performance lithium-metal battery anodes. *Adv. Mater.* **2017**, *29*, 1603755.

[38] Luo, J.; Fang, C. C.; Wu, N. L. High polarity poly(vinylidene difluoride) thin coating for dendrite-free and high-performance

lithium metal anodes. *Adv. Energy Mater.* **2018**, *8*, 1701482.
[39] Tamwattana, O.; Park, H.; Kim, J.; Hwang, I.; Yoon, G.; Hwang, T. H.; Kang, Y. S.; Park, J.; Meethong, N.; Kang, K. High-dielectric polymer coating for uniform lithium deposition in anode-free lithium batteries. *ACS Energy Lett.* **2021**, *6*, 4416–4425.
[40] Lopez, J.; Pei, A.; Oh, J. Y.; Wang, G. J. N.; Cui, Y.; Bao, Z. N. Effects of polymer coatings on electrodeposited lithium metal. *J. Am. Chem. Soc.* **2018**, *140*, 11735–11744.
[41] He, Y. T.; Zhang, Y. H.; Sari, H. M. K.; Wang, Z. H.; Lü, Z.; Huang, X. Q.; Liu, Z. G.; Zhang, J. J.; Li, X. F. New insight into Li metal protection: Regulating the Li-ion flux via dielectric polarization. *Nano Energy* **2021**, *89*, 106334.
[42] Meyerson, M. L.; Papa, P. E.; Heller, A.; Mullins, C. B. Recent developments in dendrite-free lithium-metal deposition through tailoring of micro- and nanoscale artificial coatings. *ACS Nano* **2021**, *15*, 29–46.
[43] Wei, J. J.; Zhu, L. Intrinsic polymer dielectrics for high energy density and low loss electric energy storage. *Prog. Polym. Sci.* **2020**, *106*, 101254.
[44] Ayala, J.; Ramirez, D.; Myers, J. C.; Lodge, T. P.; Parsons, J.; Alcoutlabi, M. Performance and morphology of centrifugally spun Co_3O_4/C composite fibers for anode materials in lithium-ion batteries. *J. Mater. Sci.* **2021**, *56*, 16010–16027.
[45] Li, J. H.; Shao, X. S.; Zhou, Q.; Li, M. Z.; Zhang, Q. Q. The double effects of silver nanoparticles on the PVDF membrane: Surface hydrophilicity and antifouling performance. *Appl. Surf. Sci.* **2013**, *265*, 663–670.
[46] Awan, S. U.; Hasanain, S. K.; Bertino, M. F.; Jaffari, G. H. Effects of substitutional Li on the ferromagnetic response of Li co-doped ZnO: Co nanoparticles. *J. Phys.: Condens. Matter* **2013**, *25*, 156005.
[47] Su, D. W.; Cortie, M.; Wang, G. X. Fabrication of N-doped graphene-carbon nanotube hybrids from prussian blue for lithium-sulfur batteries. *Adv. Energy Mater.* **2017**, *7*, 1602014.
[48] Zhang, L. H.; Yin, X. G.; Shen, S. B.; Liu, Y.; Li, T.; Wang, H.; Lv, X. H.; Qin, X. Y.; Chiang, S. W.; Fu, Y. Z. et al. Simultaneously homogenized electric field and ionic flux for reversible ultrahigh-areal-capacity Li deposition. *Nano Lett.* **2020**, *20*, 5662–5669.
[49] Wang, G.; Chen, C.; Chen, Y. H.; Kang, X. W.; Yang, C. H.; Wang, F.; Liu, Y.; Xiong, X. H. Self-stabilized and strongly adhesive supramolecular polymer protective layer enables ultrahigh-rate and large-capacity lithium-metal anode. *Angew. Chem., Int. Ed.* **2020**, *59*, 2055–2060.
[50] Zhang, W. D.; Wu, Q.; Huang, J. X.; Fan, L.; Shen, Z. Y.; He, Y.; Feng, Q.; Zhu, G. N.; Lu, Y. Y. Colossal granular lithium deposits enabled by the grain-coarsening effect for high-efficiency lithium metal full batteries. *Adv. Mater.* **2020**, *32*, 2001740.
[51] Fu, C. Y.; Venturi, V.; Kim, J.; Ahmad, Z.; Ells, A. W.; Viswanathan, V.; Helms, B. A. Universal chemomechanical design rules for solid-ion conductors to prevent dendrite formation in lithium metal batteries. *Nat. Mater.* **2020**, *19*, 758–766.
[52] Yu, Z. A.; Wang, H. S.; Kong, X.; Huang, W.; Tsao, Y.; Mackanic, D. G.; Wang, K. C.; Wang, X. C.; Huang, W. X.; Choudhury, S. et al. Molecular design for electrolyte solvents enabling energy-dense and long-cycling lithium metal batteries. *Nat. Energy* **2020**, *5*, 526–533.
[53] Zhan, Y. X.; Shi, P.; Ma, X. X.; Jin, C. B.; Zhang, Q. K.; Yang, S. J.; Li, B. Q.; Zhang, X. Q.; Huang, J. Q. Failure mechanism of lithiophilic sites in composite lithium metal anode under practical conditions. *Adv. Energy Mater.* **2022**, *12*, 2103291.
[54] Di, J.; Yang, J. L.; Tian, H.; Ren, P. F.; Deng, Y. R.; Tang, W. H.; Yan, W. Q.; Liu, R. P.; Ma, J. M. Dendrites-free lithium metal anode enabled by synergistic surface structural engineering. *Adv. Funct. Mater.* **2022**, *32*, 2200474.
[55] Zhu, J. Q.; Cui, Z.; He, S. A.; Wang, H.; Gao, M. L.; Wang, W. Q.; Yang, J. M.; Xu, X. T.; Hu, J. Q.; Lu, A. J. et al. Inorganic-rich and flexible solid–electrolyte interphase formed over dipole–dipole interaction for highly stable lithium-metal anodes. *Adv. Funct. Mater.* **2022**, *32*, 2205304.
[56] Zhang, S. J.; You, J. H.; He, Z. W.; Zhong, J. J.; Zhang, P. F.; Yin, Z. W.; Pan, F.; Ling, M.; Zhang, B. K.; Lin, Z. Scalable lithiophilic/sodiophilic porous buffer layer fabrication enables uniform nucleation and growth for lithium/sodium metal batteries. *Adv. Funct. Mater.* **2022**, *32*, 2200967.